J. Fluid Mech. (1980), *vol.* 99, *part* 4, *pp.* 725–738
Printed in Great Britain

Stability of the conduction regime of natural convection in a tall vertical annulus

By INN G. CHOI AND SEPPO A. KORPELA
Department of Mechanical Engineering, The Ohio State University, Columbus, Ohio 43210

(Received 21 September 1979 and in revised form 25 January 1980)

The stability of natural convection in a vertical annular enclosure has been studied by the linear theory. It was found that for all Prandtl numbers the instability sets in as a wave travelling upward. For low Prandtl numbers, the larger the curvature the more stable the flow; the reverse is true for high Prandtl numbers. The theoretical predictions of the mode of instability were verified for air. A multicellular flow pattern was observed to drift upward with the predicted wave speed. The measured wavelength of the cells is in good agreement with the linear analysis.

1. Introduction

This article is on stability of convection in a tall annular enclosure with the inner wall heated and the outer one cooled. The temperature difference between the side walls causes the fluid inside the cavity to circulate, with fluid rising adjacent to the hot wall and sinking next to the cold one. The motion can be shown to depend on the Rayleigh number, the Prandtl number, the aspect ratio h of the cavity (the height to width ratio), and the ratio of the inner and outer radii. When the radius ratio approaches unity the cavity becomes rectangular. In this case, from the studies of Batchelor (1954), Eckert & Carlson (1961), Elder (1965), and Gill (1966), the following trends are known to hold.

Near the mid-height of a tall enclosure the flow is parallel to the side walls for sufficiently small Rayleigh numbers. This parallel-flow region extends further towards the ends of the enclosure the smaller the Rayleigh number or the larger the aspect ratio. When the flow is parallel, heat is transferred across the gap by conduction alone, and the flow is said to be in the conduction regime. Gill & Davey (1969) proposed that this will be so whenever $Ra \leqslant 300h$. It is not clear how low a value h may have while this equation remains valid, but to produce a flow which turns around and becomes parallel it would seem that h should be at least, say, 3.

An increase in the temperature difference across a narrow cavity filled with a low-Prandtl-number fluid causes the parallel flow to undergo a transition to a multicellular flow pattern. If the aspect ratio is low however, and the Prandtl number is large, the vertical flow begins to take the form of boundary layers near the side walls. In this case the flow is said to enter a convection regime in which, in addition to the boundary layers, a stable vertical temperature gradient develops in the core of the flow. A further increase in the temperature difference causes the flow in the convection

† Present address: Technical Center, Owens-Corning Fiberglas, Granville, Ohio 43023.

0022–1120/80/4505–1690 $02.00 © 1980 Cambridge University Press

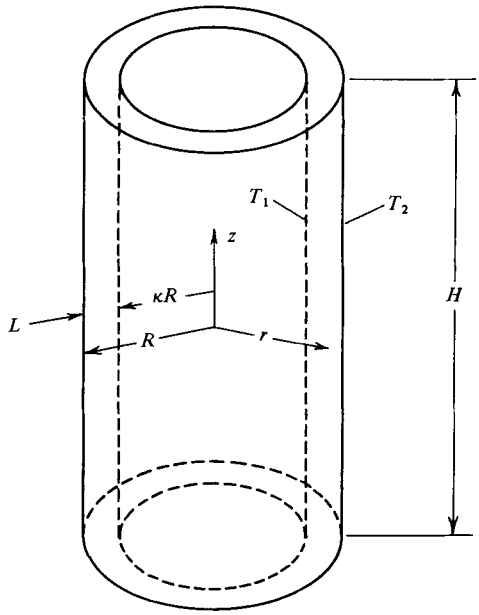

FIGURE 1. Schematic of the annular geometry.

regime to undergo a transition to a multicellular flow as well. Both of these transitions have been observed in experiments (Elder 1965; Vest & Arpaci 1969) and the linear stability theory has been used to predict them. Owing to the simplicity of the base flow, the onset of instability of the flow in the conduction regime can be determined accurately (Gershuni 1953; Rudakov 1967; Birikh *et al.* 1972; Korpela, Gözüm & Baxi 1973). This is not the case for the transition from the convection regime because of the uncertainty of the exact magnitude of the vertical temperature gradient. But, if this gradient is treated parametrically, much can be learned about the stability of this flow (Gill & Davey 1969; Hart 1971; Bergholz 1978).

In engineering applications the stability of these flows is important in determining the insulating capacity of the rectangular regions they occupy, for in the multicellular flow regime the increased heat transfer, as a result of a unit increase in the difference between the temperatures of the vertical walls, ought to be larger than the corresponding change when the fluid flows in a unicellular manner. Although a rectangular enclosure is most likely to be found in practice, annular regions are also common and thus the stability of convection in such regions is also of interest.

In this article results from a linear stability analysis of the flow in an annular enclosure with a heated inner wall are presented. The annulus is taken to be sufficiently tall that the flow will be in the conduction regime. Thus complications arising from a vertical temperature stratification are ignored and the emphasis is on the effect of the wall curvature on the stability. In addition to theoretical calculations, visual observations of the flow were made and photographs taken of the streaks left by smoke particles in air.

2. Formulation and solution

Consider the flow of a viscous fluid within an annular enclosure, as shown in figure 1, of height H, inner radius κR and outer radius R, with $H/R_m \gg 1$, and $H/L \gg 1$, where R_m is the average of the two radii and L is the width of the annular gap. The flow results from a temperature of the inner cylinder T_1 being higher than that of the outer one T_2. A cylindrical co-ordinate system is chosen with the positive z axis in the direction opposite to the gravity vector $\mathbf{g}$. The temperature difference $\Delta T = T_1 - T_2$ is assumed sufficiently small so that the Oberbeck–Boussinesq approximation applies (Chandrasekhar 1961, page 16). Accordingly the kinematic viscosity ν, thermal diffusivity α, and the coefficient of thermal expansion β, are constant and the work of compression and viscous dissipation can be neglected.

For an infinitely tall annulus the base flow is parallel and can be readily obtained. The radial distribution of the axial velocity and temperature are given by

$$\frac{\overline{w}}{U} = \frac{1}{16(1-\kappa)^2}\left\{\left[\frac{(1-\kappa^2)(1-3\kappa^2)-4\kappa^4\ln\kappa}{(1-\kappa^2)^2+(1-\kappa^4)\ln\kappa}\right]\left[(1-\kappa)^2\left(\frac{r}{L}\right)^2-1\right.\right.$$
$$\left.\left.+(1-\kappa^2)\frac{\ln((1-\kappa)(r/L))}{\ln\kappa}\right]-4\left[\left(\frac{r}{L}\right)^2(1-\kappa)^2-\kappa^2\right]\frac{\ln((1-\kappa)(r/L))}{\ln\kappa}\right\}, \tag{1}$$

and

$$\frac{\overline{T}}{\Delta T} = \frac{\ln((1-\kappa)(r/L))}{\ln\kappa}, \tag{2}$$

in which $L = R(1-\kappa)$ is the width of the annular gap, $U = g\beta L^2\Delta T/\nu$ is the characteristic thermal velocity, and $\overline{T} = T - T_2$ is the difference between the fluid temperature and that of the outer wall. It was found convenient in later calculations to introduce a new radial co-ordinate $\zeta = [r - \frac{1}{2}(1+\kappa)R]/L$ which is measured from the mid-plane of the gap. The non-dimensional base velocity and temperature profiles are shown in terms of this co-ordinate in figure 2.

Choosing, as in equations (1) and (2), U, ΔT and L as the scales for velocity, temperature, and length and scaling time by L^2/ν and pressure by ρU^2, where ρ is the density, the governing equations can be cast in the following non-dimensional forms:

$$\nabla.\mathbf{q} = 0, \tag{3}$$

$$\frac{\partial\mathbf{q}}{\partial t} + G(\mathbf{q}.\nabla)\mathbf{q} = -G\nabla p + T\hat{\mathbf{z}} + \nabla^2\mathbf{q}, \tag{4}$$

$$\frac{\partial T}{\partial t} + G(\mathbf{q}.\nabla)T = \frac{1}{P}\nabla^2 T. \tag{5}$$

In these equations $\mathbf{q}$ is the non-dimensional velocity and T the non-dimensional temperature measured relative to its value at the outer wall. The non-dimensional pressure is measured above the hydrostatic value. The parameters $G = UL/\nu$ and $P = \nu/\alpha$ are the Grashof and Prandtl number respectively, and $\hat{\mathbf{z}}$ is a unit vector in the positive z direction.

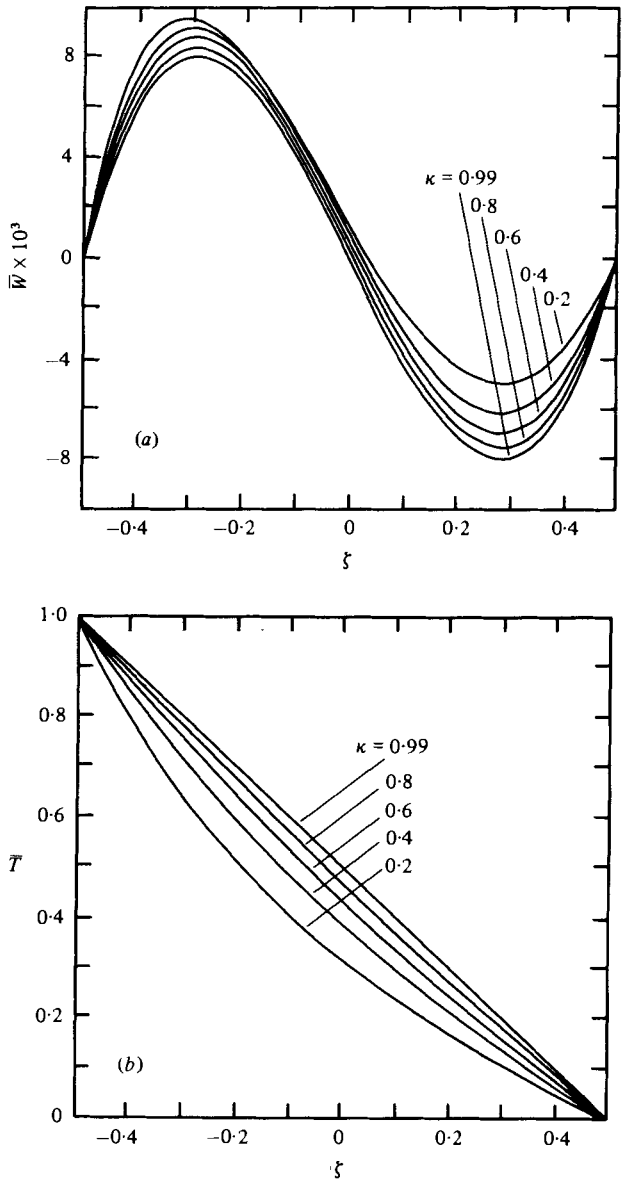

FIGURE 2. (a) Base flow velocity profiles and (b) base flow temperature profiles for various values of the inner to outer radius ratio κ.

Subtracting the base solutions from equations (3)–(5) and linearizing the resulting equations yields

$$\nabla . \mathbf{q}' = 0, \tag{6}$$

$$\frac{\partial \mathbf{q}'}{\partial t} + G\bar{w}\frac{\partial \mathbf{q}'}{\partial z} + GD\bar{w}(\hat{\mathbf{r}} . \mathbf{q}')\hat{\mathbf{z}} = -G\nabla p' + T'\hat{\mathbf{z}} + \nabla^2 \mathbf{q}', \tag{7}$$

$$\frac{\partial T'}{\partial t} + G\bar{w}\frac{\partial T'}{\partial z} + GD\bar{T}(\hat{\mathbf{r}} . \mathbf{q}') = \frac{1}{P}\nabla^2 T', \tag{8}$$

subject to boundary conditions

$$\mathbf{q}' = T' = 0 \quad \text{at} \quad r = \kappa/(1-\kappa),\ 1/(1-\kappa), \tag{9}$$

in which a prime denotes that the variable is a perturbation on the base flow, which is denoted by a bar. As is conventional $D = \partial/\partial r$.

In observing the flow only axisymmetric motions were seen. For this reason in what follows the disturbances are also assumed to be axisymmetric. Thus their spatial dependence can be written as

$$\phi'(r,z,t) = \phi(r,t)\exp(i\alpha z), \tag{10}$$

where ϕ' represents any of the dependent variables. Eliminating the pressure leads to

$$\frac{\partial}{\partial t}(DD^*-\alpha^2)u + i\alpha G\left[\bar{w}(DD^*-\alpha^2)+\frac{1}{r}D\bar{w}-D^2\bar{w}\right]u = -i\alpha DT + (DD^*-\alpha^2)^2 u, \tag{11}$$

$$\frac{\partial T}{\partial t} + i\alpha G\bar{w}T + GD\bar{T}u = \frac{1}{P}(D^*D-\alpha^2)T \tag{12}$$

and

$$u = D^*u = T = 0 \quad \text{at} \quad r = \kappa/(1-\kappa) \text{ and } 1/(1-\kappa), \tag{13}$$

where $D^* = D + 1/r$, and $u = \hat{\mathbf{r}}.\mathbf{q}$ is the amplitude of the radial perturbation velocity.

The eigenvalue problem (11)–(13) was solved by the Galerkin method. Following Walowit, Tsao & DiPrima (1964), polynomials which satisfy the boundary conditions (13) were used as trial functions. These are

$$u_n(\zeta) = (\zeta^2-\tfrac{1}{4})^2\zeta^{n-1}, \tag{14}$$

$$T_n(\zeta) = (\zeta^2-\tfrac{1}{4})\zeta^{n-1}, \tag{15}$$

where $\zeta = r - \frac{1}{2}[(1+\kappa)/(1-\kappa)]$; thus $r = \kappa/(1-\kappa)$ and $1/(1-\kappa)$ correspond to $\zeta = -\frac{1}{2}$ and $+\frac{1}{2}$, respectively. Rewriting the equations (11) and (12) in terms of the co-ordinate ζ, substituting the expansions

$$u(\zeta,t) = \sum_{n=1}^{\infty} a_n(t)\,u_n(\zeta) \tag{16}$$

and

$$T(\zeta,t) = \sum_{n=1}^{\infty} b_n(t)\,T_n(\zeta) \tag{17}$$

into the resulting set, truncating each of the series to N terms, and requiring the residuals to be orthogonal to the trial functions with the weight

$$\zeta + \tfrac{1}{2}(1+\kappa)/(1-\kappa)]$$

yields the matrix equation

$$\mathbf{A}\frac{d\{\mathbf{X}\}}{dt} + \mathbf{B}\mathbf{X} = 0. \tag{18}$$

In this equation $\mathbf{X} = \{a_n, b_n\}^T$ is the transpose of the coefficient vector, and $\mathbf{A}$ and $\mathbf{B}$ are matrices with complex elements resulting from the orthogonalization. The matrix eigenvalue problem (18) was solved by the complex QR algorithm.

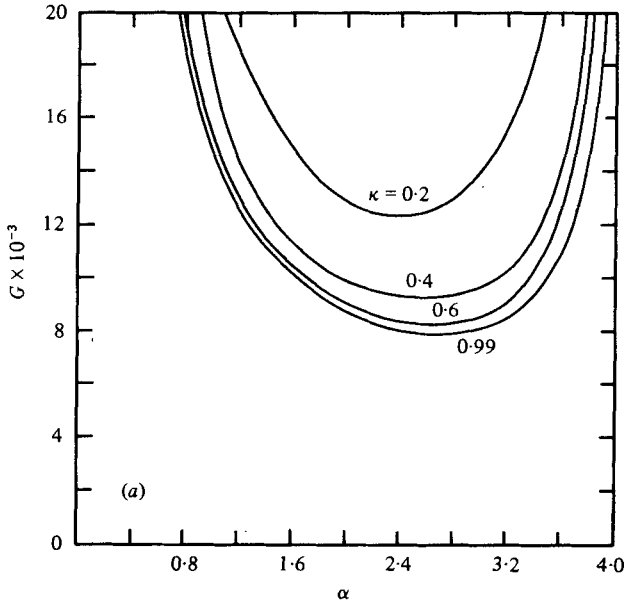

FIGURE 3 (a). For legend see p. 733.

3. Results

In carrying out the computations by the Galerkin method success depends on how well the eigenfunctions can be approximated by a small number of terms in the series of trial functions. As was noted by DiPrima (1955), in the absence of a critical layer the eigenfunctions do not oscillate rapidly so that the series can be truncated to only a few terms. This situation was encountered in natural convection in a Cartesian slot (Korpela *et al.* 1973) for low Prandtl numbers, for the instability then sets in as stationary convection. Eight-term expansion in that case was sufficient to determine the critical Grashof number to four significant figures. The convergence deteriorated with an increase in Prandtl number, for, unlike the case at low Prandtl numbers when the convergence slows with increased αG, for $P > 1$ the rate of convergence depends on how large the product αGP is. For large Prandtl numbers instability has been found by Gill & Kirkham (1970) to set in as oscillations at a substantially lower value of Grashof number than at low values of P. For this case ten terms were necessary to assure convergence to 0·5 % of the actual critical Grashof number.

With this experience on the calculation of the stability of natural convection in a rectangular cavity, the computations reported here for convection in an annulus were expected to lead to nearly equally fast convergence. This was true except in a range of intermediate values of Prandtl number. In particular, in the range

$$P < 1 \quad \text{and} \quad 15 < P < 1000$$

twelve terms with the present set of trial functions was adequate for equally good convergence as in the study of natural convection in a rectangular slot. In the intermediate range $1 < P < 15$, the convergence deteriorated rapidly and reliable results could not be obtained.

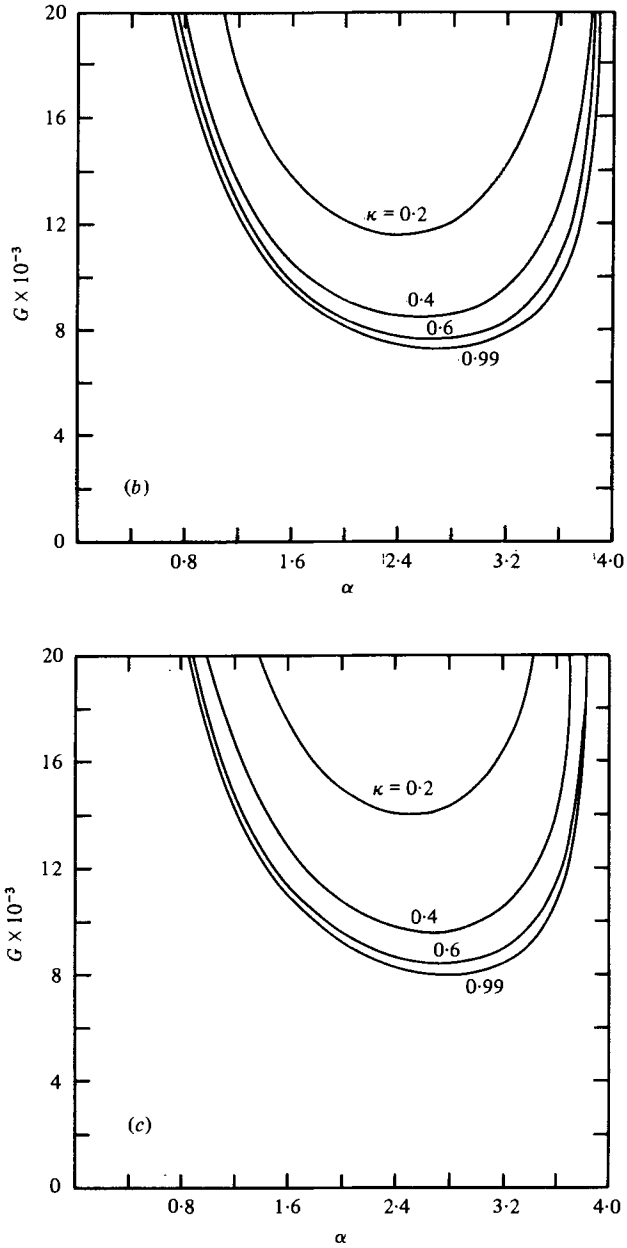

FIGURE 3 (*b*, *c*.) For legend see p. 733.

The neutral states for six values of Prandtl number and four or five inner to outer radius ratios are shown in figure 3. The neutral states for the radius ratio $\kappa = 0{\cdot}99$ correspond closely to the values for the Cartesian case. Since at low values of Prandtl number the temperature disturbances become unimportant the instability is sustained by energy being transferred to the disturbance from the base flow. This shear flow type of instability is also present in the inviscid limit owing to an inflexion point in the velocity profiles. Thus the neutral curves are open as $G \to \infty$, as shown.

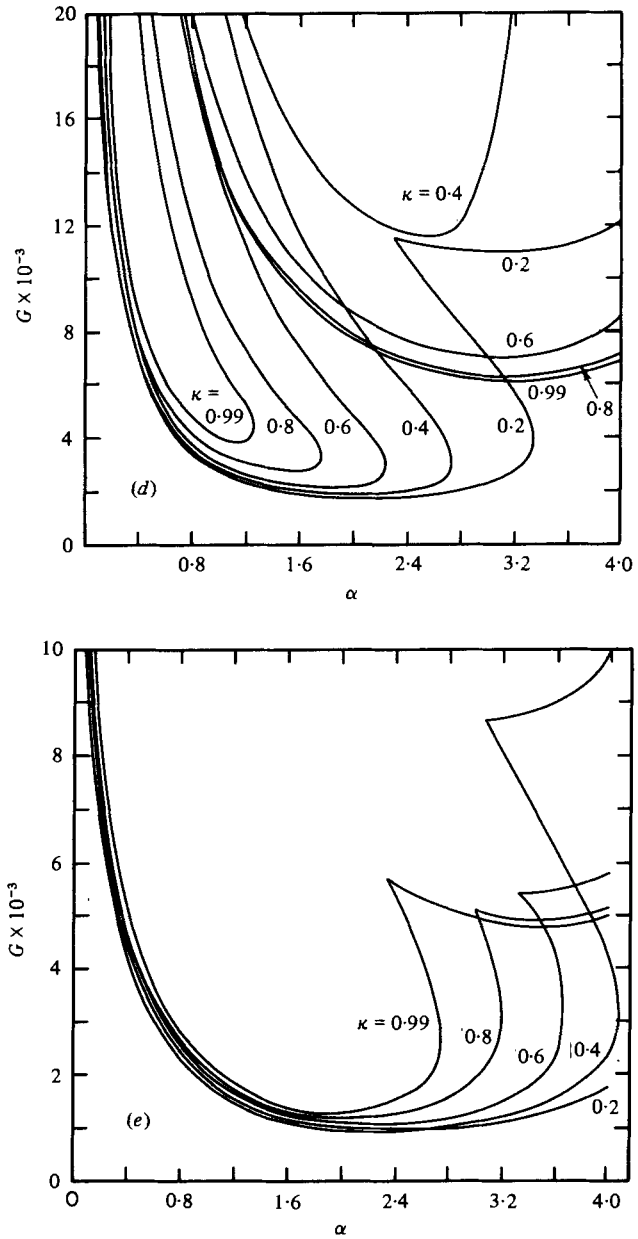

FIGURE 3 (*d*, *e*). For legend see p. 733.

From the results of Hart (1971) it can be concluded that for the flow here considered at high values of Prandtl number (figures 3*d*–*f*) more of the kinetic energy of the disturbance comes from the potential energy of the buoyancy field, although this is still less than that derived from the base flow. The neutral stability curves (figure 3*d*) for $P = 15$ show this buoyant mode as well as the shear type. For $P = 35$ the shear mode is still partially present but disappears from the graphs at $P = 100$ for the values of α and G investigated. At $P = 15$ the radius ratio has a marked effect on both the

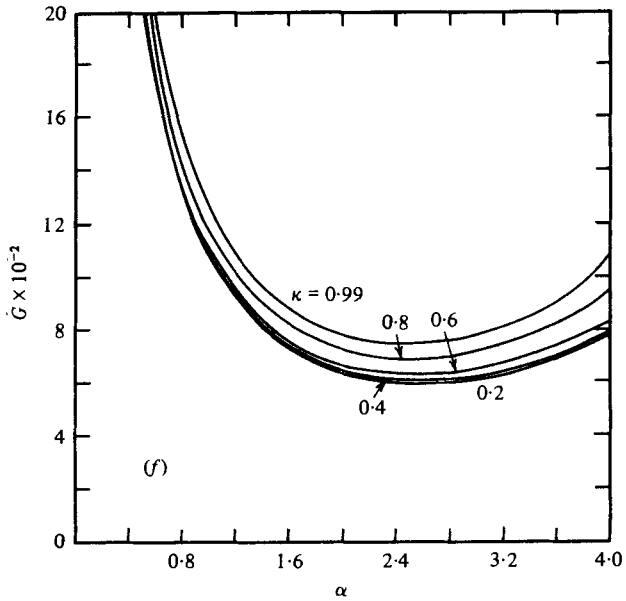

FIGURE 3. Neutral states for various values of κ. (*a*) $P = 0$; (*b*) $P = 0{\cdot}1$; (*c*) $P = 0{\cdot}71$; (*d*) $P = 15$; (*e*) $P = 35$; (*f*) $P = 100$.

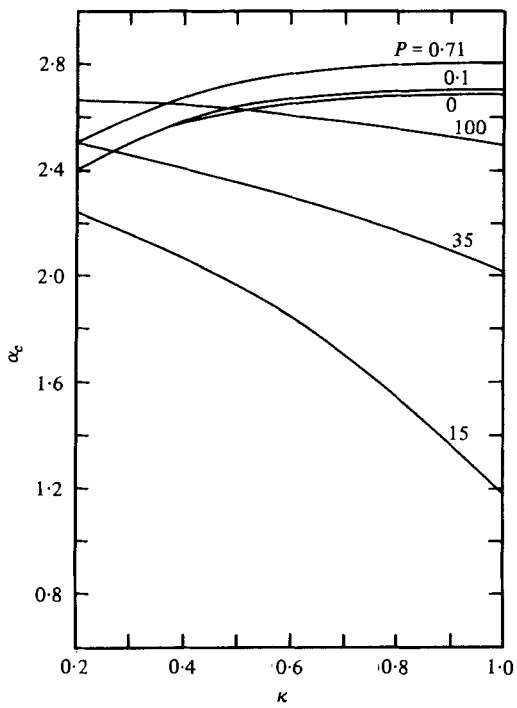

FIGURE 4. The critical wavenumbers for various values of P as functions of the radius ratio κ.

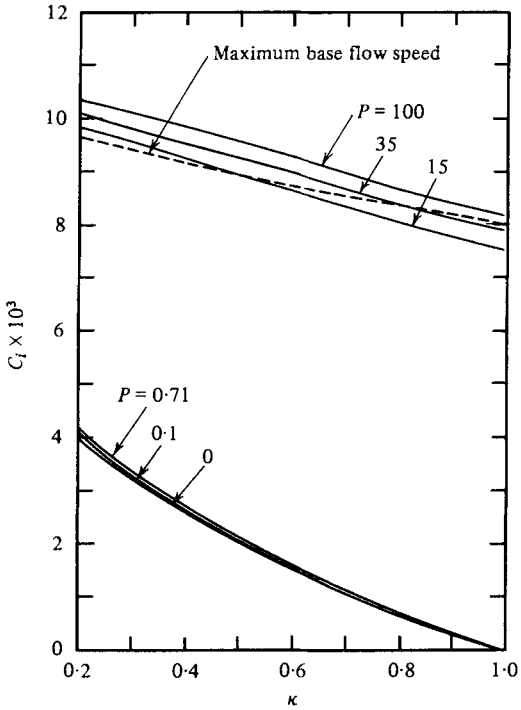

FIGURE 5. The critical wave speeds for various values of P as functions of the radius ratio κ.

critical Grashof number and the wavelength of the unstable mode; for $P = 35$ and 100 these are largely absent. The neutral curves are quite flat near the minimum and curiously the curve for $\kappa = 0{\cdot}4$ has a lower minimum than the curves for $\kappa = 0{\cdot}2$ and $\kappa = 0{\cdot}6$ when $P = 35$.

The critical wavenumbers are shown in figure 4. The effect of curvature on the critical wavenumber at low Prandtl numbers is seen to be opposite to that at $P > 15$, but except in the range $15 \leqslant P \leqslant 50$ and $0{\cdot}8 \leqslant \kappa \leqslant 1$, when the wavelength of the critical mode can be as large as five times the width of the annular gap, for other values of P and κ the variation of the critical wavelength with both P and κ is rather weak and its value is approximately 2·5 times the gap width.

The wave speeds at low and high values of Prandtl number are consistent with what has been found in the Cartesian case. In that situation the odd symmetry of the base flow suggests that the instability should set in either as stationary convection, or as a pair of travelling waves which could result in a standing wave pattern. Stationary multicellular convection has been found in the rectangular cavity for $P \leqslant 12{\cdot}7$ and two waves travelling in opposite directions for $P > 12{\cdot}7$. The low Prandtl number result is in agreement with experiments, but no experiments which would show a transition from the conduction regime for high Prandtl numbers have been carried out, for the reason that these experiments would require an aspect ratio of the order of a thousand. The two travelling waves which appear at the onset of instability have a wave speed which is close to the maximum base flow speed. The waves are the kind which arise from the critical layers. These layers are far apart, symmetrically located

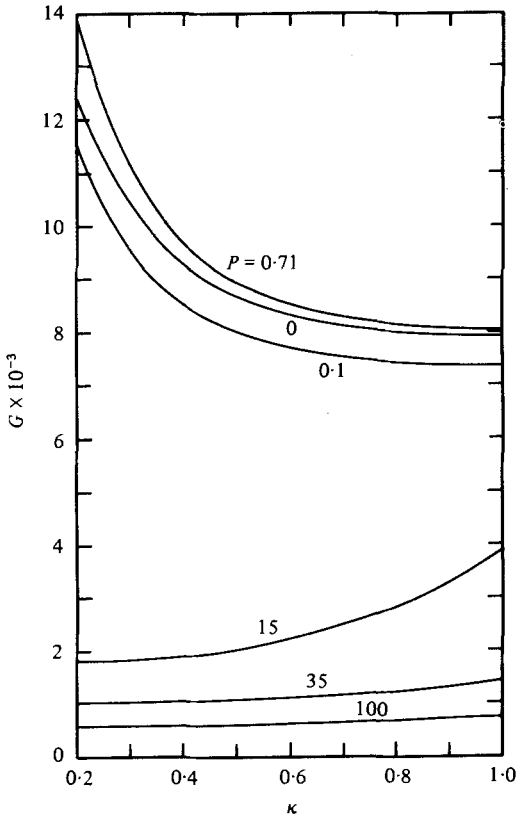

FIGURE 6. The states of neutral stability for various values of P as functions of the radius ratio κ.

about the vertical mid-plane of the cavity. Thus the two waves are unlikely to interact in a way which would result in a standing wave pattern.

With the introduction of curvature the stationary cellular pattern, characteristic of low-Prandtl-number flows, begins to drift upward in the direction opposite to gravity. The speed of travel, shown in figure 5, is quite independent of the Prandtl number but increases as the radius ratio is decreased. For high Prandtl numbers one of the two oppositely travelling waves at the critical layers is damped at the onset of instability, and a single wave, again travelling in the direction opposite to gravity, remains. This is a consequence of the odd symmetry of the base solutions being destroyed and the type of degeneracy which was present in the Cartesian case being removed by the curved walls.

The Grashof numbers of the neutral states are shown graphically in figure 6. Their numerical values together with the critical wavenumbers and wave speeds are summarized in table 1. The effect of curvature in the low-Prandtl-number range is to stabilize the flow, for air by nearly a factor of two as κ decreases from unity to 0·2. In the high-Prandtl-number range the opposite is true and the flow is destabilized as κ becomes smaller, although at $Pr = 100$ the effect is very small.

P		κ = 0·99	0·8	0·6	0·4	0·2
0	G_c	7931	8004	8320	9232	12408
	α_c	2·69	2·69	2·65	2·58	2·40
	c_r	~ 0	$0{\cdot}67 \times 10^{-3}$	$1{\cdot}51 \times 10^{-3}$	$2{\cdot}59 \times 10^{-3}$	$4{\cdot}00 \times 10^{-3}$
0·1	G_c	7350	7418	7710	8561	11594
	α_c	2·71	2·70	2·67	2·59	2·40
	c_r	~ 0	$0{\cdot}69 \times 10^{-3}$	$1{\cdot}54 \times 10^{-3}$	$2{\cdot}65 \times 10^{-3}$	$4{\cdot}11 \times 10^{-3}$
0·71	G_c	8038	8126	8512	9658	13912
	α_c	2·81	2·80	2·77	2·68	2·50
	c_r	~ 0	$0{\cdot}70 \times 10^{-3}$	$1{\cdot}57 \times 10^{-3}$	$2{\cdot}69 \times 10^{-3}$	$4{\cdot}17 \times 10^{-3}$
15	G_c	3875	2810	2227	1906	1814
	α_c	1·18	1·54	1·85	2·06	2·24
	c_r	$7{\cdot}57 \times 10^{-3}$	$8{\cdot}06 \times 10^{-3}$	$8{\cdot}64 \times 10^{-3}$	$9{\cdot}27 \times 10^{-3}$	$9{\cdot}82 \times 10^{-3}$
35	G_c	1443	1275	1137	1057	1053
	α_c	2·02	2·18	2·31	2·41	2·50
	c_r	$7{\cdot}92 \times 10^{-3}$	$8{\cdot}38 \times 10^{-3}$	$8{\cdot}99 \times 10^{-3}$	$9{\cdot}58 \times 10^{-3}$	$10{\cdot}10 \times 10^{-3}$
100	G_c	750	686	628	599	612
	α_c	2·50	2·56	2·60	2·65	2·66
	c_r	$8{\cdot}21 \times 10^{-3}$	$8{\cdot}66 \times 10^{-3}$	$9{\cdot}25 \times 10^{-3}$	$9{\cdot}83 \times 10^{-3}$	$10{\cdot}32 \times 10^{-3}$

TABLE 1. Summary of the critical states.

4. Experiment

For the purpose of observing the flow an annular cavity was constructed by placing an aluminium cylinder concentrically inside a Plexiglas one and both fitted with a common Plexiglas top and bottom. The cavity thus formed was 90·8 cm tall and 2·34 cm wide, for an aspect ratio of 38·6. The outer diameter of the enclosure was 14·9 cm and the inner one 10·2 cm so that the radius ratio was 0·68. Three cylindrical heaters, each with separately controllable level of power, were placed inside the aluminium cylinder. The cylinder itself was instrumented with fifteen 24-gauge iron–constantan thermocouples, each secured into its own well by aluminium cement. The thermocouple wells, which were deep enough to be within 0·05 cm of the outer surface of the 0·8 cm thick aluminium cylinder, were spaced uniformly 15·25 cm apart in the vertical directions and 120° apart circumferentially. To maintain the walls at uniform temperature the bottom of the apparatus was insulated with 7·6 cm thick styrofoam. A 8·9 cm thick layer of fibreglass was used to insulate the top. The measured non-uniformity in the surface temperature was at most 0·6 °C. Three cardboard panels surrounded the apparatus to reduce the influence of air currents; the fourth side was left open for observations.

A Carousel slide projector was used as a source of light to illuminate a vertical plane of the annulus. An attempt was made to orient the slit forming the sheet of light in such a way that the illuminated plane would also contain the axis of the annulus. The fluid particles were made visible by introducing cigar smoke into the annulus.

In figure 7 (plate 1) four photographs of the flow, taken with a Nikon-F 35 mm camera on Kodak Tri-X (ASA 400) film, are shown. The first photograph, with $G = 7400$, corresponds to the flow in the conduction regime before the onset of instability. In the second photograph $G = 9100$. The flow consists of cells which are $5{\cdot}4 \pm 0{\cdot}1$ cm apart and drift upward with a velocity $0{\cdot}76 \pm 0{\cdot}04$ cm s^{-1}. These values correspond to a non-dimensional wavenumber equal to 2·72 and a non-dimensional wave speed equal to $1{\cdot}24 \times 10^{-3}$. As the Grashof number is increased to 12600 the flow becomes distorted as shown in the third photograph and the wavelength is larger than at the onset of instability. The flow is still regular whereas in the last photograph it is seen to become irregular (and also unsteady) as the Grashof number has been increased to 21200.

Two more photographs are included. In figure 8 (plate 2) a detail of a cell, as it has reached the top end, is shown. The yardstick on the side provides a visual reference of the physical size of the cells and the apparatus. The cells as they reach the end region at the top are quickly destroyed. Away from the ends the flow is mainly vertical with a slight periodic variation in the amplitude of the vertical velocity. This periodicity, together with a small periodic transverse component of velocity, produces the cellular stream pattern. Upon reaching the end the main flow becomes two-dimensional and the cells disappear, leaving the streamlines in the end region only slightly distorted from what they would be if the cells were not present. This description is based not only on our observations of the flow but on numerical experiments which we will present in the future.

The figure 9 (plate 2) is a photograph from the top end of the annulus. Although it is of poor quality, it is good enough to show that the flow is axisymmetric. Neither the thickness, nor the centre of the smoke band changes in the angular direction. The

outer band is the true image of the smoke; the inner one is its reflexion from the inner aluminium cylinder.

5. Conclusion

The stability of the conduction regime of natural convection in a vertical annulus has been predicted by using linearized equations. The flow, at low Prandtl numbers, was shown to undergo a transition to a multicellular pattern which drifts upward. Both the wavelength of the cells and their upward velocity are in good agreement with visual observations of the flow. When the gap width of the annulus becomes small in comparison to the mean radius the predictions agree also with those published for a vertical slot. At high Prandtl numbers the instability sets in as a wave which travels upward with the ascending flow near the inner cylinder, at the speed which is close to the maximum of the base flow. Experiments to verify this instability require an annulus of very large aspect ratio, and none have been carried out. The only experiments for high-Prandtl-number fluids in a vertical annulus for which instability has been observed are those of Elder (1965). He found toroidal cells as we did, but these were stationary. His results correspond to a transition from a convection regime.

The study here reported formed part of a Ph.D. dissertation of I. G. Choi. The support of the National Science Foundation through grant ENG 76-18426 is gratefully acknowledged, as is the use of the Amdahl 470 V/6-II computer of the Instruction and Research Computer Center of the Ohio State University.

REFERENCES

Batchelor, G. K. 1954 *Quart. Appl. Math.* **12**, 209.

Bergholz, R. F. 1978 *J. Fluid Mech.* **84**, 743.

Birikh, R. V., Gershuni, G. Z., Zhukhovitskii, E. M. & Rudakov, R. N. 1972 *Prikl. Math. Mech.* **36**, 707.

Chandrasekhar, S. 1961 *Hydrodynamic and Hydromagnetic Stability*. Oxford University Press.

DiPrima, R. C. 1955 *Quart. Appl. Math.* **16**, 55.

Eckert, E. R. G. & Carlson, W. O. 1961 *Int. J. Heat Mass Transfer* **2**, 106.

Elder, J. W. 1965 *J. Fluid Mech.* **23**, 77.

Gershuni, G. Z. 1953 *Zh. Tech. Fiz.* **23**, 1838.

Gill, A. E. 1966 *J. Fluid Mech.* **26**, 515.

Gill, A. E. & Davey, A. 1969 *J. Fluid Mech.* **35**, 775.

Gill, A. E. & Kirkham, C. C. 1970 *J. Fluid Mech.* **42**, 125.

Hart, J. 1971 *J. Fluid Mech.* **47**, 547.

Korpela, S. A., Gözüm, D. & Baxi, C. B. 1973 *Int. J. Heat Mass Transfer* **16**, 1683.

Rudakov, R. N. 1967 *Prikl. Math. Mech.* **31**, 376.

Vest, C. M. & Arpaci, V. S. 1969 *J. Fluid Mech.* **36**, 1.

Walowit, J., Tsao, S. & DiPrima, R. C. 1964 *J. Appl. Mech.* **31**, 585.

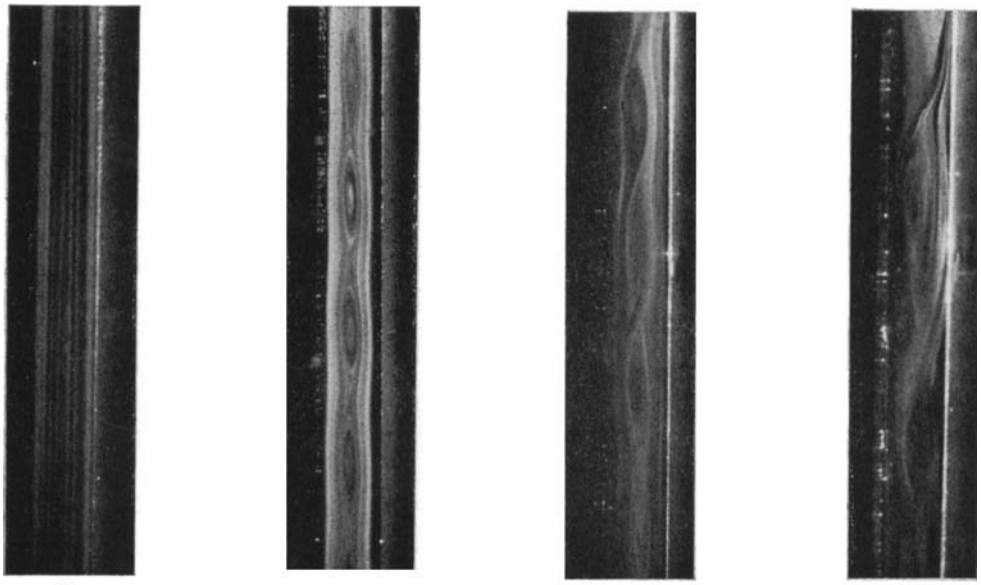

(*a*) (*b*) (*c*) (*d*)

FIGURE 7. Multicellular convection in an annulus. (*a*) $G = 7400$; (*b*) $G = 9100$; (*c*) $G = 12600$; (*d*) $G = 21200$.

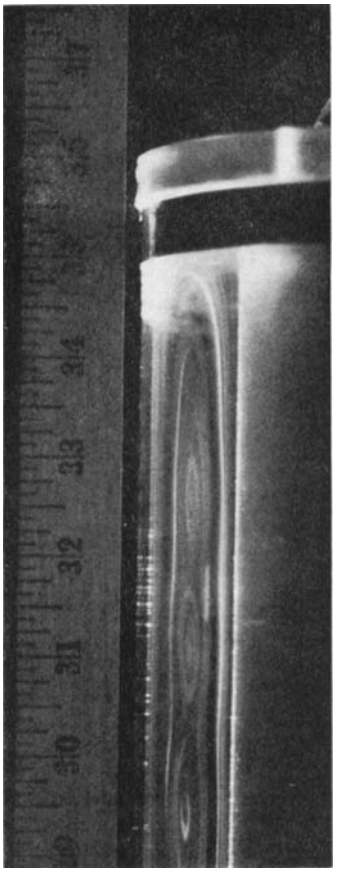

FIGURE 8. End region of the cavity.

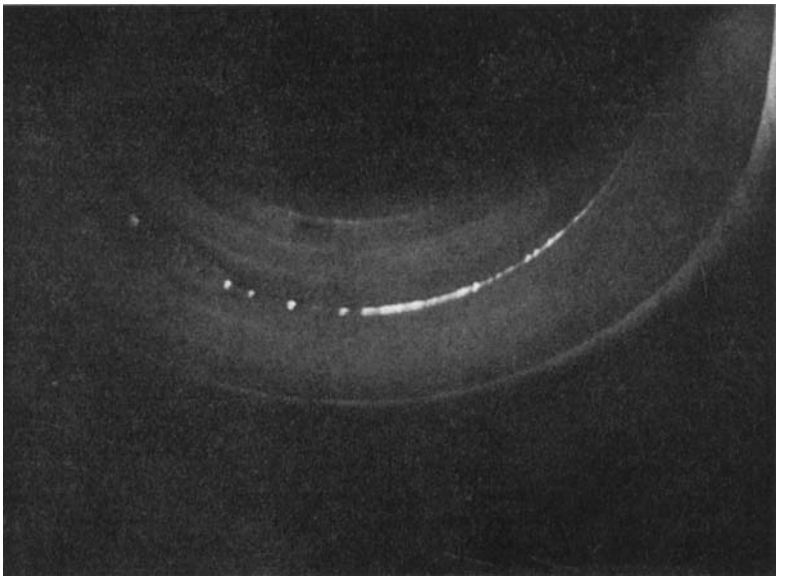

FIGURE 9. View from the top of axisymmetric convection.